Supporting Information

Large-Area and Broadband Thermoelectric Infrared Detection in a Carbon Nanotube Black-Body Absorber

Mingyu Zhang[1], Dayan Ban[2], Chao Xu[2], and John T.W. Yeow[1]*

1 Advanced Micro-/Nano-Devices Lab, Department of Systems Design Engineering, University of Waterloo, 200 University Avenue West, Waterloo, Ontario N2L 3G1, Canada

2 Waterloo Institute for Nanotechnology and Department of Electrical and Computer Engineering, University of Waterloo, 200 University Avenue West, Waterloo, Ontario, N2L 3G1, Canada

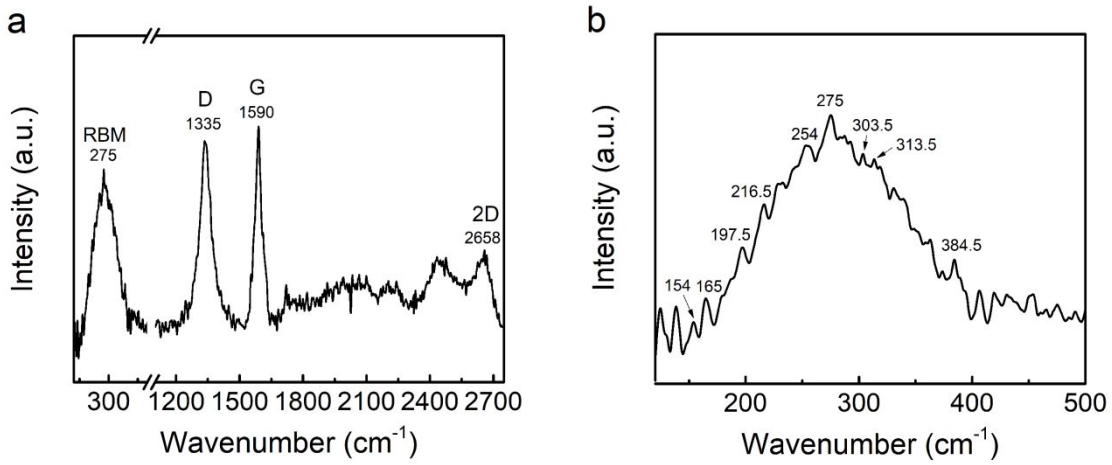

Figure S1. Raman spectrum of CNTF. a) A full Raman spectrum indicating the RBM peak (275 cm^{-1}), D peak (1335 cm^{-1}), G peak (1590 cm^{-1}), and 2D peak (2658 cm^{-1}). b) The amplified RBM peak group containing several small peaks.

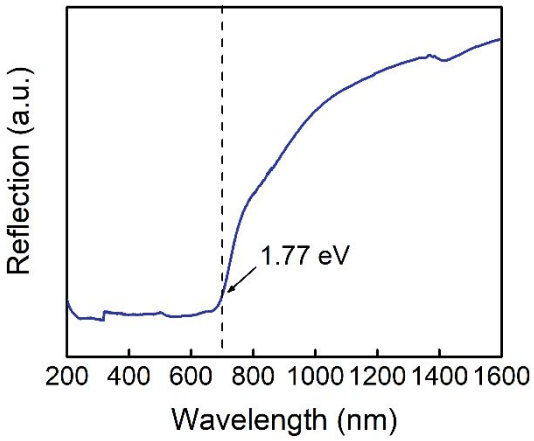

Figure S2. The UV-Vis spectrum of CNTF. The reflection increase at longer wavelength is due to reduced light absorption as the photon energy becomes smaller than the bandgap energy of a portion of CNTs. The onset at 700 nm corresponds to the bandgap of 1.77 eV.

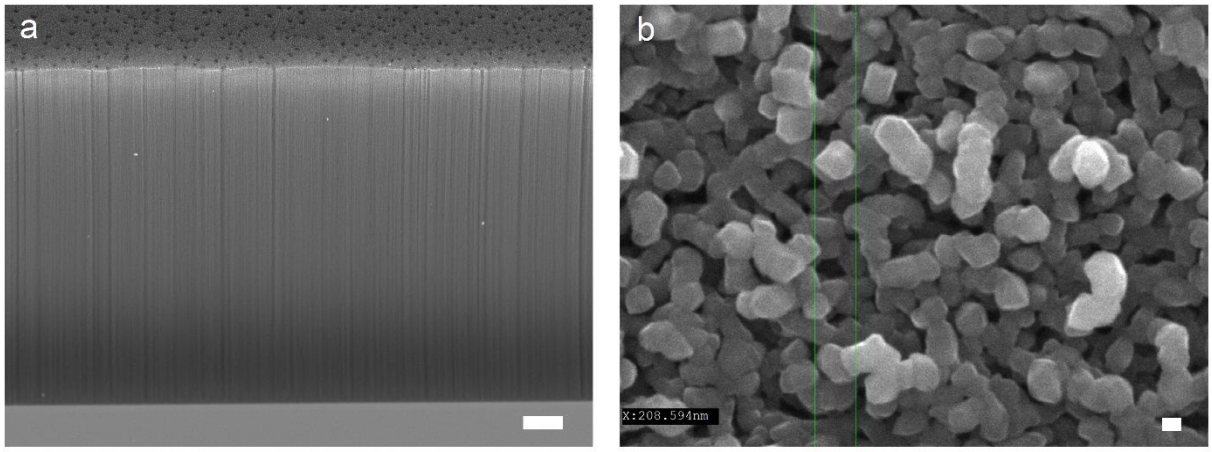

Figure S3. Morphologies of a CNTF and a metal covered CNTF. a) Tilt-viewed SEM image of pristine CNTF with 110 μm height. Scale bar is 10 μm. b) Top-viewed SEM image of a 200 nm Al covered CNTF. The diameter of each individual CNT expands to ~209 nm after Al sputtering. With the knowledge that pristine CNTs diameter is 8~10 nm, the actual metal coverage (~100 nm) on each CNT is in fact half of the sputtered thickness. Scale bar is 100 nm.

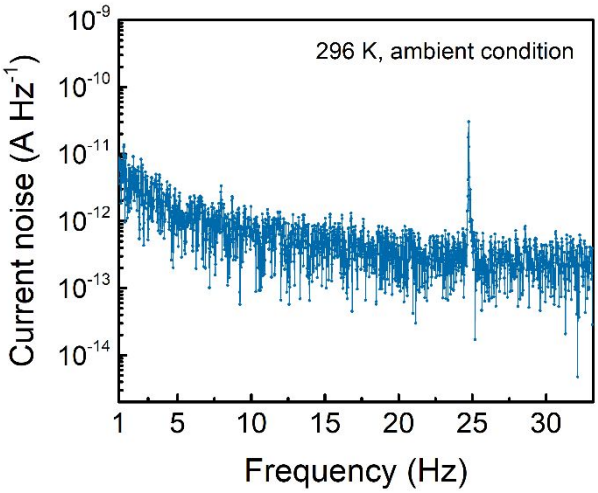

Figure S4. Measured zero-biased current noise at 296 K under ambient condition in the 25 nm Al covered CNTF detector with 0.05 mm^{-2} area. The sharp peak near 25 THz repeatedly occurs in each measuremnt which is thus considered to be the noise from measurement system.

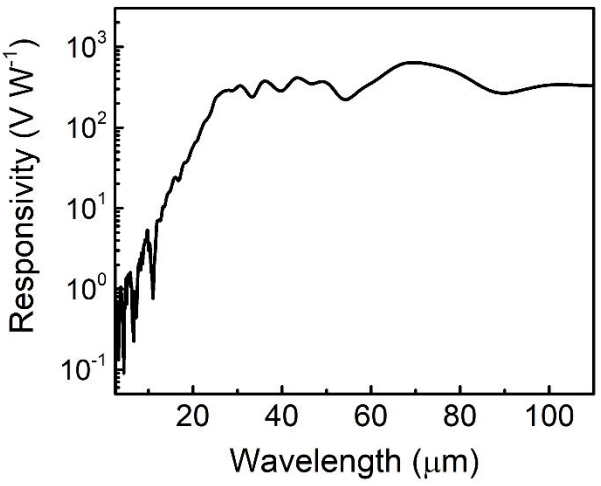

Figure S5. The wavelength dependent photoresponsivity at zero-bias of the CNTF detector (25 nm thick Al and 0.05 mm^2 device area) in a broad spectral range. The R_V exhibits a peak of 640 V W^{-1} at 70 μm wavelength. It is noted that the NEP and detectivity correlations with wavelength are determined by the pronounced variation of photo responsivity R_V. The noise level in our device is independent of incident light wavelength.

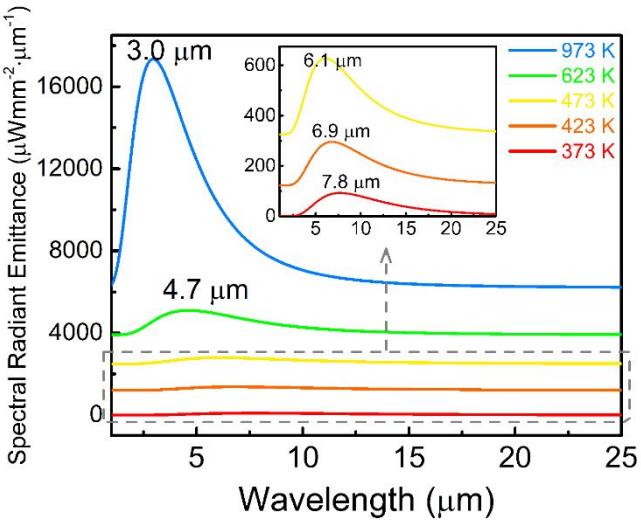

Figure S6. Calculated black-body spectral radiant emittances at temperature of 373 K, 423 K, 473 K, 623 K, and 973 K. The peak wavelength of the emittance spectrum increases from 3.0 μm to 7.8 μm as the blackbody radiative temperature decreases from 973 K to 373 K.

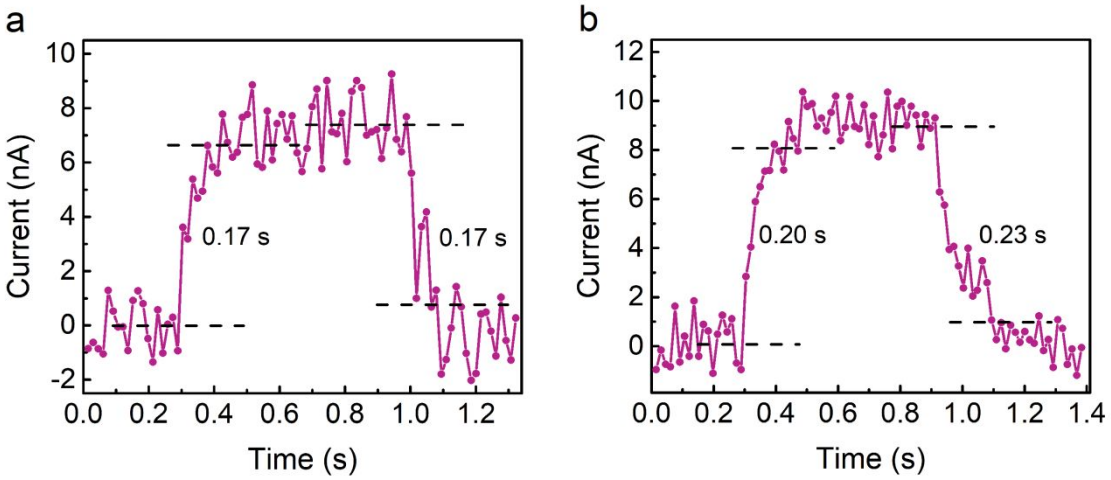

Figure S7. Detector rise and fall times characterized by a) a blackbody radiation source at 973 K (~90 μW mm^{-2}, peak wavelength 3 μm) and b) a blackbody radiation beam (~350 μW mm^{-2}) filtered by a THz window (cut-off frequency at 15 THz).

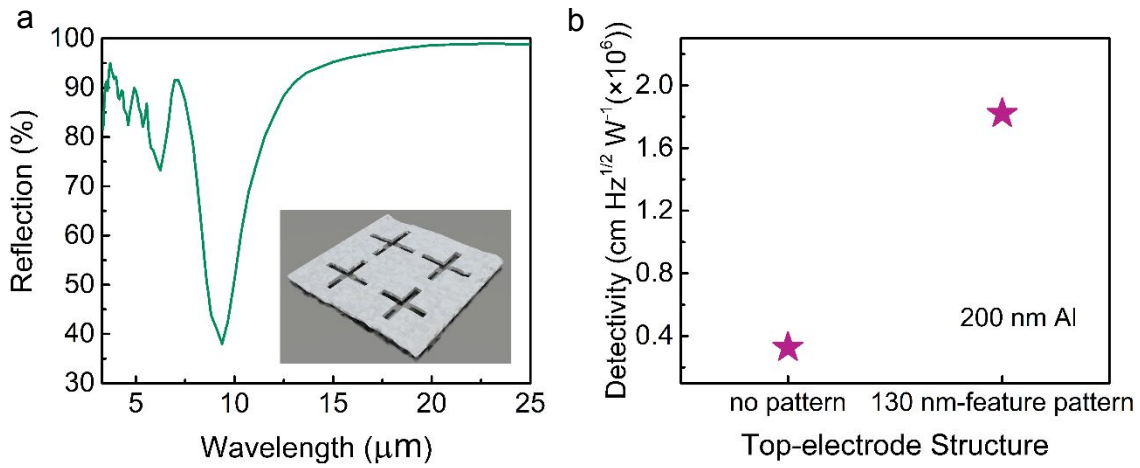

Figure S8. A CNTF photodetector with electron-beam lithography (EBL) patterned Al top-electrode. a) Simulated reflectance spectrum of a CNTF detector covered by 200 nm Al with periodic cross-shape pattern. The reflection dip is designed to be 9.3 μm, which is identical to infrared radiation from a human body, demonstrating the capability of a photodetector for body temperature monitoring and harvesting. The inset shows the schematic diagram of the patterns. Each period (3.7 μm) consists of 4 crosses with the same width of 130 nm, but diffrent lengths: 1.67 μm (left top), 1.60 μm (right top), 1.53 μm (left bottom), and 1.46 μm (right bottom). The patterns are chosen to reduce the light reflection at the designed wavelength. Here, the SEM image of the pattern is not shown to avoid the damaging and doping effect by high-energy electrons at high-resolution mode.[1] b) Photoresponse comparison of a CNTF photodetector with and without the periodic patterns, showing a 5 times improvement.

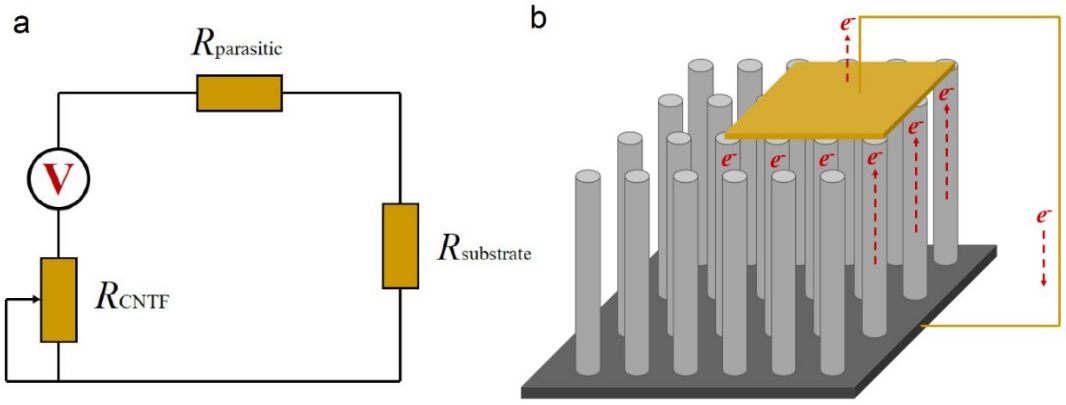

Figure S9. Equivalent circuit of the photodetector. The Al covered CNTF acts as a voltage power source, and the whole resistance of the device is the sum of three resistances: $R_{parasitic}$, $R_{substrate}$, and R_{CNTF}. While the PTE voltage is relatively constant as photosensitive area decreases ($V = \int S(z)\nabla T(z)dz$), an increase in device resistance has been measured: 644 Ω in 6 mm^2 device, 1084 Ω in 1 mm^2 device, and 2369 Ω in 0.05 mm^2 device. This is because less individual CNTs are involved in charge transport among circuit-loop after CNTF lateral size has been reduced. This leads to an increase in electrical resistance and a reduction in overall photocurrent simultaneously.

Table S1. Comparison between this work and representative PTE photodetectors.

Photosensitive Materials	Photosensitive area	Light-source power	Responsive wavelength	Responsivity	NEP	Detectivity	Ref.
Metal covered CNTF	0.05 mm^2	6.8 μW mm^{-2}	2.5~25 μm 7.8 μm peak	5.3 V W^{-1}	1 nW $Hz^{-1/2}$	1.9×10^7 cm $Hz^{1/2}$ W^{-1}	This work
			4.3 THz	640 V W^{-1}	8.4 pW $Hz^{-1/2}$	2.3×10^9 cm $Hz^{1/2}$ W^{-1}	
Antenna based graphene	λ^2/π	2.3 μW	2.52 THz	105 V W^{-1}	80 pW $Hz^{-1/2}$	-	2
CNT film	-	2.6 mW	1.4 THz	-	2.4 nW $Hz^{-1/2}$	-	3
Black phosphorus	7.2 μm^2	325 μW	0.26~0.38 THz	0.15 V W^{-1}		-	4
Nanoporous silicon	100 mm^2	500 μW mm^{-2}	476~514 nm	-		-	5
Bi_2Te_3/Sb_2Te_3 nanowires	0.0025 mm^2	10^4 μW mm^{-2}	0.5~0.75 μm	38 V W^{-1}		6.1×10^5 cm $Hz^{1/2}$ W^{-1}	6
$SrTiO_3$	planar junction	≥11.6 mW	0.33~10.67 μm	1.18 V W^{-1}		-	7
Graphene	<1 μm^2	10 μW	0.5~0.9 μm	0.12 V W^{-1}		-	8
Graphene ribbons	4.2 μm^2	0.75 μW	119 μm	10 V W^{-1}		~2×10^6 cm $Hz^{1/2}$ W^{-1}	9
CNT fiber *p-n* junction	*p-n* junction	-	0.41~ 216 μm	0.17 V W^{-1}		2.2×10^6 cm $Hz^{1/2}$ W^{-1}	10
Graphene *p-n* junction	several μm^2	~10^2 μW	0.45~1.55 μm	0.19 V W^{-1}		-	11

Table S2. Physical properties of four CNTF/top-electrode junctions.

Junction Properties	Al	Ti	Au	ITO
Seebeck coefficient	-1.7 μV K^{-1}	9.1 μV K^{-1}	1.9 μV K^{-1}	-29 μV K^{-1}
Thermal barrier resistance with CNTs[12]	0.81	0.74	1.06	-
Electrical contact resistance with CNTs[13–15]	Low	Low	Medium	High

Note: The Seebeck coefficient of CNTs are usually in the range of 20~50 μV K^{-1}.

Table S3. Infrared thermometer measured and calculated device temperature under global illumination of IR source.

Temperature		Device top surface	Substrate sidewall	Measured ΔT	Calculated ΔT
Illumination Power	90 μW mm^{-2}	29.1 ℃	28.4 ℃	0.7 ℃	0.26 ℃
	350 μW mm^{-2}	32.0 ℃	31.1 ℃	0.9 ℃	0.42 ℃

Note: The device temperature without illumination is measured to be 23.2 ℃ in ambient conditions.

Note S1: Raman, UV-Vis spectra, and chirality of CNTF

As shown in Figure S1, the Raman spectrum of CNTF exhibits radial breathing mode (RBM) peak, D peak, G peak, and 2D peak. The combined appearances of G peak and 2D peak confirm the characteristic graphitic sp^2 hybridization and the D peak represents the structural disorders. The RBM peak is the signature of carbon nanotubes (CNTs) especially single-walled CNTs, and one can obtain the information on CNT chirality by analyzing the RBM position.[16] Since we have not used methods to control the chirality deliberately, the CNTF in this work is a mixture of metallic CNTs and semiconducting CNTs.[17] The RBM peak at 154 cm^{-1}, 165 cm^{-1}, 197.5 cm^{-1}, 216.5 cm^{-1}, 254 cm^{-1}, 275 cm^{-1}, 303.5 cm^{-1}, 313.5 cm^{-1}, 384.5 cm^{-1} correspond to CNT diameters of 1.62 nm, 1.53 nm, 1.26 nm, 1.14 nm, 0.96 nm, 0.88 nm, 0.77 nm, 0.79 nm, 0.62 nm,[18] and chirality of (16, 7) - metallic, (11, 11) - metallic, (11, 7)/(14, 3), (12, 4), (8, 6), (10, 2), (9, 1), (10, 0), (5, 4), respectively.[19] The highest RBM peak at 275 cm^{-1} corresponds to the richest content of (10, 2) type CNTs with 0.88 nm diameter and 1.18 eV energy bandgap.[19] The onset of reflection increase in UV-Vis spectrum indicates that the largest bandgap of CNTs with various chirality is 1.77 eV as shown in Figure S2.

The chirality of CNTs can affect the PTE responsivity mainly in terms of thermoelectric conversion rather than light absorption process because of the bandgap limitless intra-band excitation mechanism. It is generally considered that metallic CNTs have lower Seebeck coefficient than semiconductor CNTs.[20–22] Therefore, the mixture of metallic and semiconducting CNTs probably have not maximized the thermoelectric effect in our CNTF, and removing the metallic CNTs would possibly further improve the detector responsivity. However, Ichinose *et al.* have recently discovered that by tuning Fermi level to the Van Hove singularity in metallic CNTs can significantly improve the Seebeck effect,[23] which provides another path to possibly improve the PTE effect without any sorting.

Note S2: Seebeck coefficient of metal thin films

An asymptotic expression of pure metal Seebeck coefficient at room temperature between the thin-film (S_{thin}) and bulk (S_{bulk}) morphologies can be given by the free-electron size effect theory:[24]

$$S_{thin} = S_{bulk}\left[1-\frac{3}{8}\left(\frac{l}{t}\right)(1-p)\frac{U}{1+U}\right] \quad \text{(S1)}$$

Where t is metal thickness, l is electron mean free path, p is the fraction of carriers reflected at the film surface specularly, and $U=\left(\frac{\partial \ln l}{\partial \ln E}\right)_{E=\varepsilon}$ where ε is the Fermi level. By assuming $P=0$, $l=100$,and $U=2$ ($i.e.\ l \propto E^2$) according to Bloch quantum theory, a notable reduction of S_{thin} compared to S_{bulk} is measured when the metal thickness is below 30 nm,[24] which is well consistent with our results.

Note S3: Noise in detector

Noise is an important consideration in evaluating photodetectors since noise levels could be quite different in various devices. The main noises considered in photodetectors include shot noise, flicker noise, and Johnson-Nyquist noise. Shot noise is caused by the fact that electrical currents are carried by discrete charges which transport randomly and discontinuously. The quantum nature of photons also leads to a statistical randomness of arrivals onto the detector surface, contributing to the fluctuation of electron-hole pair generation.[25] Shot noise can be described as

$$i_{sh} = \sqrt{2eI_{DC}\Delta f} \quad \text{(S2)}$$

where e is the electron charge, I_{DC} is the average DC current, and Δf is the instrument bandwidth. Because shot noise obviously increases with current, high-voltage biased

photodetectors often suffer from significant shot noises. Flicker noise is also referred as pink noise or $1/f$ noise because this kind of noise is proportional to $1/f^a$ where $0 < a < 2$ and more pronounced in low frequency regime. Flicker noise is generally accepted to arise from the fluctuation of carrier concentration (in semiconductors) and mobility (in metals) due to the presence of defects and disorders as trapping and scattering sites.[26] The flicker noise in graphene and carbon nanotubes are found to scale with current and temperature.[26,27]

Johnson-Nyquist noise (thermal noise) is the random voltage fluctuation existing in all electronic devices due to the thermodynamic motion of carriers. The Johnson-Nyquist noise level is expressed as

$$V_{JN} = \sqrt{4k_B T \Delta f R} \tag{S3}$$

where k_B is the Boltzmann constant, T is the temperature of the electronic device, and R is the resistance of the whole circuit.

Given the consideration that our PTE detector operates under zero bias, the shot noise and flicker noise are significantly reduced. The reduced noise is a useful merit to self-powered (zero-biased) photodetectors in achieving high photo detectivity, and also an important reason for sensitive room-temperature detection in mid- and far- infrared regimes.

Note S4: Elevated photoresponse in THz range

We explain the strong photoresponse dependence on wavelength with two physical mechanisms: 1) the plasmon resonance enhanced light absorption in THz range which leads to higher thermal gradient in CNTs, and 2) the weak electron- phonon coupling which leads to less significant hot-carrier relaxation under low-energy photon excitation.

It is widely accepted that light absorption of individual CNT varies a lot throughout the broadband infrared spectrum. For the span from near-infrared to far-infrared, the light absorption shows a dip in mid-infrared region (2~10 μm) due to Pauli blocking, and a

broadband, significant peak in far-infrared region (at ~75 μm, 4 THz) due to plasmon resonance.[28–32] Now let us consider the light absorption in the CNTF scenario. By virtue of strong light trapping effect within the forest (multiple reflections and transmissions), CNTF exhibits constant and high absorbing characteristic in a broad spectral range as shown in Figure 2e and ref.[33]. However, the light penetration depths into the forest could be quite different at different wavelengths attributed to its wavelength selectivity.[34] Therefore, because the intrinsic light absorption in CNTs is higher in far infrared or THz region, the electromagnetic waves and photon induced hot-carriers are better confined at the very top part of CNTF. This gives rise to a higher temperature asymmetry along the CNTs and thus enhanced thermoelectric effect which accounts for the elevated photoresponse.

Cai *et al*. also reported a lower PTE photoresponse at shorter wavelength comparing to the long-wavelength THz range.[9] They attributed it to the negative effect of optical phonon emission which leads to quick thermal relaxation of hot electrons in graphene. When the incident photon energy is lower than the optical and zone-boundary phonon energy of CNTs (~0.16 eV), we think the weak electron-phonon coupling[9,35,36] have induced less significant hot-carrier relaxation which helps maintain a fairly high thermal gradient. This mechanism could also contribute to the elevated PTE effect of the detector in the THz range.

Note S5: Device temperature gradient

As shown in Table S2, we found as illumination power density increases, the substrate is heated up simultaneously with CNTF top surface, leading to a non-linear temperature gradient increase and non-linear photoresponsivity shown in Fig. 3B. This is because the CNTF are still too short for effective heat dissipation, and the silicon substrate is seated on a thermally insolating Teflon board which lacks effective cooling. Therefore, a more rational choice of substrate material and additional bottom cooling layer are preferred to further improve device performance.

The Calculated ΔT is estimated by $V = \int S \nabla T$ assuming S_{CNTF} = 30 μV K^{-1}. The difference between measured ΔT and calculated ΔT is probably caused by two reasons: 1) the relatively large measurement focal spot size of infrared thermometer compared to the device vertical dimension, 2) the emissivity difference between CNTs and silicon,[33] which leads to inevitable errors in non-contact measurement.

Note S6: The effect of diameter, density, and mobility of CNTs on detector PTE effect

The detector performance would also be optimized in smaller diameter, higher density, and higher carrier mobility CNTF.

The diameter of CNTs is found correlated to thermoelectric effect.[37,38] When the tube diameter decreases, the CNT bandgap is enlarged and the carrier concentration is reduced. As a result, the Seebeck coefficient is improved as explained by[39]

$$S = \frac{8L}{h^2} m^* T \left(\frac{\pi}{3n} \right)^{2/3} \quad \text{(S4)}$$

where $L = \pi^2 k_B^{\,2} / 3e^2$ is the Lorentz number, h is Planck constant, m^* is effective mass of the carrier, and n is carrier concentration. From another perspective, enhanced quantum confinement effect in lower physical dimension (smaller diameter) will lead to a larger energy derivative of density of states,[37,40] which could also contribute to the thermoelectric efficiency.

The increase of CNT density is considered to optimize the photo detectivity by increasing photocurrent and reducing resistance. As illustrated in Figure 8S, under certain temperature gradient and thermoelectric voltage, the more individual CNT involved in the circuit, more current the device will output. This means the resistance of the detector is reduced as a result of increased cross-section. Assuming Johnson noise is the dominant noise, when CNT density

is increased at a given photosensitive area (the same received incident power), the photo detectivity will therefore be improved due to $D^* \propto 1/\sqrt{R}$.[6,41]

The effect of carrier mobility on detector performance can be understood in two aspects. First, the figure of merit for thermoelectric materials - *ZT* value is described as

$$ZT = \frac{\sigma S^2 T}{\kappa} \tag{S5}$$

where σ is electrical conductivity, κ is thermal conductivity, *S* is Seebeck coefficient, and *T* is temperature. Since the Seebeck coefficient is correlated with electrical conductivity ($\sigma = ne\mu$) *via* carrier concentration *n* rather than carrier mobility μ (equation S4), the mobility will monotonously affect the electrical conductivity but not Seebeck coefficient.[42] So enhanced mobility can improve the *ZT* value of thermoelectric materials. Second, enhanced mobility, *i.e.* reduced resistance is considered to reduce the noise level in PTE detector and thus improve the photo detectivity.[6,41] The electrical resistance is $R = R_{sub} + R_{para} + R_{CNTF}$, and $R_{CNTF} = \rho H / A = H / Ane\mu$ where *H*, *A* are the height and area of CNTF. By assuming Johnson-Nyquist noise $V_{JN} = \sqrt{4k_B TR}$ is the dominant noise type, the detectivity can be put as

$$D^* = \sqrt{A} R_V / V_{JN} = \sqrt{A} \int S \nabla T / \sqrt{4k_B TR} \tag{S6}$$

Therefore, enhanced mobility would improve the photo detectivity by reducing electrical resistance.

References

(1) Yu, X.; Dong, Z.; Yang, J. K. W.; Wang, Q. J. Room-Temperature Mid-Infrared Photodetector in All-Carbon Graphene Nanoribbon-C60 Hybrid Nanostructure. *Optica* **2016**, *3*, 979–984.

(2) Castilla, S.; Terrés, B.; Autore, M.; Viti, L.; Li, J.; Nikitin, A. Y.; Vangelidis, I.; Watanabe, K.; Taniguchi, T.; Lidorikis, E.; Vitiello, M. S.; Hillenbrand, R.; Tielrooij, K.-J.; Koppens, F. H. L. Fast and Sensitive Terahertz Detection Using an Antenna-Integrated Graphene *pn* Junction. *Nano Lett.* **2019**, *19*, 2765−2773.

(3) Suzuki, D.; Oda, S.; Kawano, Y. A Flexible and Wearable Terahertz Scanner. *Nat. Photonics* **2016**, *10*, 809–813.

(4) Viti, L.; Hu, J.; Coquillat, D.; Knap, W.; Tredicucci, A.; Politano, A.; Vitiello, M. S. Black Phosphorus Terahertz Photodetectors. *Adv. Mater.* **2015**, *27*, 5567.

(5) Lai, Y.-S.; Tsai, C.-Y.; Chang, C.-K.; Huang, C.-Y.; Hsiao, V. K. S.; Su, Y. O. Photothermoelectric Effects in Nanoporous Silicon. *Adv. Mater.* **2016**, *28*, 2644.

(6) Mauser, K. W.; Kim, S.; Mitrovic, S.; Fleischman, D.; Pala, R.; Schwab, K. C.; Atwater, H. A. Resonant Thermoelectric Nanophotonics. *Nat. Nanotechnol.* **2017**, *12*, 770–775.

(7) Lu, X.; Jiang, P.; Bao, X. Phonon-Enhanced Photothermoelectric Effect in SrTiO3 Ultra-Broadband Photodetector. *Nat. Commun.* **2019**, *10*, 138.

(8) Shautsova, V.; Sidiropoulos, T.; Xiao, X.; Güsken, N. A.; Black, N. C. G.; Gilbertson, A. M.; Giannini, V.; Maier, S. A.; Cohen, L. F.; Oulton, R. F. Plasmon Induced Thermoelectric Effect in Graphene. *Nat. Commun.* **2018**, *9*, 5190.

(9) Cai, X.; Sushkov, A. B.; Suess, R. J.; Jadidi, M. M.; Jenkins, G. S.; Nyakiti, L. O.; Myers-Ward, R. L.; Li, S.; Yan, J.; Gaskill, D. K.; Murphy, T. E.; Drew, H. D.; Fuhrer, M. S. Sensitive Room-Temperature Terahertz Detection *via* the Photothermoelectric Effect in Graphene. *Nat. Nanotechnol.* **2014**, *9*, 814–819.

(10) Zubair, A.; Wang, X.; Mirri, F.; Tsentalovich, D. E.; Fujimura, N.; Suzuki, D.; Soundarapandian, K. P.; Kawano, Y.; Pasquali, M.; Kono, J. Carbon Nanotube Woven Textile Photodetector. *Phys. Rev. Mater.* **2018**, *2*, 015201.

(11) Echtermeyer, T. J.; Nene, P. S.; Trushin, M.; Gorbachev, R. V; Eiden, A. L.; Milana, S.; Sun, Z.; Schliemann, J.; Lidorikis, E.; Novoselov, K. S.; Ferrari, A. C. Photothermoelectric and Photoelectric Contributions to Light Detection in Metal-Graphene-Metal Photodetectors. *Nano Lett.* **2014**, *14*, 3733–3742.

(12) Li, Q.; Liu, C.; Fan, S. Thermal Boundary Resistances of Carbon Nanotubes in Contact with Metals and Polymers. *Nano Lett.* **2009**, *9*, 3805–3809.

(13) Zienert, A.; Schuster, J.; Gessner, T. Metallic Carbon Nanotubes with Metal Contacts: Electronic Structure and Transport. *Nanotechnology* **2014**, *25*, 425203.

(14) Matsuda, Y.; Deng, W. Q.; Goddard, W. A. Contact Resistance Properties between Nanotubes and Various Metals from Quantum Mechanics. *J. Phys. Chem. C* **2007**, *111*, 11113–11116.

(15) Zhang, J.; Chia, A. C. E.; Lapierre, R. R. Low Resistance Indium Tin Oxide Contact to N-GaAs Nanowires. *Semicond. Sci. Technol.* **2014**, *29*, 054002.

(16) Kawai, M.; Kyakuno, H.; Suzuki, T.; Igarashi, T.; Suzuki, H.; Okazaki, T.; Kataura, H.; Maniwa, Y.; Yanagi, K. Single Chirality Extraction of Single-Wall Carbon Nanotubes for the Encapsulation of Organic Molecules. *J. Am. Chem. Soc.* **2012**, *134*, 9545–9548.

(17) Yang, F.; Wang, X.; Zhang, D.; Yang, J.; Luo, D.; Xu, Z.; Wei, J.; Wang, J. Q.; Xu, Z.; Peng, F.; Li, X.; Li, R.; Li, Y.; Li, M.; Bai, X.; Ding, F.; Li, Y. Chirality-Specific Growth of Single-Walled Carbon Nanotubes on Solid Alloy Catalysts. *Nature* **2014**, *510*, 522–524.

(18) Dresselhaus, M. S.; Dresselhaus, G.; Saito, R.; Jorio, A. Raman Spectroscopy of Carbon Nanotubes. *Phys. Rep.* **2005**, *409*, 47–99.

(19) Weisman, R. B.; Bachilo, S. M. Dependence of Optical Transition Energies on

Structure for Single-Walled Carbon Nanotubes in Aqueous Suspension: An Empirical Kataura Plot. *Nano Lett.* **2003**, *3*, 1235–1238.

(20) Crispin, X. Thermoelectrics: Carbon Nanotubes Get High. *Nat. Energy* **2016**, *1*, 16037.

(21) Avery, A. D.; Zhou, B. H.; Lee, J.; Lee, E.-S.; Miller, E. M.; Ihly, R.; Wesenberg, D.; Mistry, K. S.; Guillot, S. L.; Zink, B. L.; Kim, Y.-H.; Blackburn, J. L.; Ferguson, A. J. Tailored Semiconducting Carbon Nanotube Networks with Enhanced Thermoelectric Properties. *Nat. Energy* **2016**, *1*, 16033.

(22) Nakai, Y.; Honda, K.; Yanagi, K.; Kataura, H.; Kato, T.; Yamamoto, T.; Maniwa, Y. Giant Seebeck Coefficient in Semiconducting Single-Wall Carbon Nanotube Film. *Appl. Phys. Express* **2014**, *7*, 025103.

(23) Ichinose, Y.; Yoshida, A.; Horiuchi, K.; Fukuhara, K.; Komatsu, N.; Gao, W.; Yomogida, Y.; Matsubara, M.; Yamamoto, T.; Kono, J.; Yanagi, K. Solving the Thermoelectric Trade-Off Problem with Metallic Carbon Nanotubes. *Nano Lett.* **2019**, *19*, 7370–7376.

(24) Chorra, K. L. *Thin Film Phenomena*; McGraw-Hill Book Company: New York, 1969.

(25) Kasap, S. O. *Optoelectronics and Photonics: Principles and Practices, 2nd edition, International edition*; Pearson Education Limited: Harlow, 2013.

(26) Balandin, A. A. Low-Frequency 1/f Noise in Graphene Devices. *Nat. Nanotechnol.* **2013**, *8*, 549–555.

(27) Tarkiainen, R.; Roschier, L.; Ahlskog, M.; Paalanen, M.; Hakonen, P. Low-Frequency Current Noise and Resistance Fluctuations in Multiwalled Carbon Nanotubes. *Phys. E Low-Dimensional Syst. Nanostructures* **2005**, *28*, 57–65.

(28) Akima, N.; Iwasa, Y.; Brown, S.; Barbour, A. M.; Cao, J.; Musfeldt, J. L.; Matsui, H.; Toyota, N.; Shiraishi, M.; Shimoda, H.; Zhou, O. Strong Anisotropy in the Far-Infrared Absorption Spectra of Stretch-Aligned Single-Walled Carbon Nanotubes. *Adv. Mater.* **2006**, *18*, 1166–1169.

(29) Zhang, Q.; Haroz, E. H.; Jin, Z.; Ren, L.; Wang, X.; Arvidson, R. S.; Luttge, A.; Kono, J. Plasmonic Nature of the Terahertz Conductivity Peak in Single-Wall Carbon Nanotubes. *Nano Lett.* **2013**, *13*, 5991–5996.

(30) Zhukova, E. S.; Grebenko, A. K.; Bubis, A. V.; Prokhorov, A. S.; Belyanchikov, M. A.; Tsapenko, A. P.; Gilshteyn, E. P.; Kopylova, D. S.; Gladush, Y. G.; Anisimov, A. S.; Anzin, V. B.; Nasibulin, A. G.; Gorshunov, B. P. Terahertz-Infrared Electrodynamics of Single-Wall Carbon Nanotube Films. *Nanotechnology* **2017**, *28*, 445204.

(31) Low, T.; Avouris, P. Graphene Plasmonics for Terahertz to Mid-Infrared Applications. *ACS Nano* **2014**, *8*, 1086–1101.

(32) Komatsu, N.; Gao, W.; Chen, P.; Guo, C.; Babakhani, A.; Kono, J. Modulation-Doped Multiple Quantum Wells of Aligned Single-Wall Carbon Nanotubes. *Adv. Funct. Mater.* **2017**, *27*, 1606022.

(33) Mizuno, K.; Ishii, J.; Kishida, H.; Hayamizu, Y.; Yasuda, S.; Futaba, D. N.; Yumura, M.; Hata, K. A Black Body Absorber from Vertically Aligned Single-Walled Carbon Nanotubes. *PNAS* **2009**, *106*, 6044–6047.

(34) Selvakumar, N.; Krupanidhi, S. B.; Barshilia, H. C. Carbon Nanotube-Based Tandem Absorber with Tunable Spectral Selectivity: Transition from Near-Perfect Blackbody Absorber to Solar Selective Absorber. *Adv. Mater.* **2014**, *26*, 2552–2557.

(35) Park, J. Y.; Rosenblatt, S.; Yaish, Y.; Sazonova, V.; Üstunel, H.; Braig, S.; Arias, T. A.; Brouwer, P. W.; McEuen, P. L. Electron-Phonon Scattering in Metallic Single-Walled Carbon Nanotubes. *Nano Lett.* **2004**, *4*, 517–520.

(36) Javey, A.; Guo, J.; Paulsson, M.; Wang, Q.; Mann, D.; Lundstrom, M.; Dai, H. High-Field Quasiballistic Transport in Short Carbon Nanotubes. *Phys. Rev. Lett.* **2004**, *92*, 10–13.

(37) Hung, N. T.; Nugraha, A. R. T.; Hasdeo, E. H.; Dresselhaus, M. S.; Saito, R. Diameter

Dependence of Thermoelectric Power of Semiconducting Carbon Nanotubes. *Phys. Rev. B* **2015**, *92*, 1–7.

(38) Hayashi, D.; Ueda, T.; Nakai, Y.; Kyakuno, H.; Miyata, Y.; Yamamoto, T.; Saito, T.; Hata, K.; Maniwa, Y. Thermoelectric Properties of Single-Wall Carbon Nanotube Films: Effects of Diameter and Wet Environment. *Appl. Phys. Express* **2016**, *9*, 025102.

(39) Snyder, G. J.; Toberer, E. S. Complex Thermoelectric Materials. *Nat. Mater.* **2008**, *7*, 105–114.

(40) Dresselhaus, M. S.; Chen, G.; Tang, M. Y.; Yang, R.; Lee, H.; Wang, D.; Ren, Z.; Fleurial, J. P.; Gogna, P. New Directions for Low-Dimensional Thermoelectric Materials. *Adv. Mater.* **2007**, *19*, 1043–1053.

(41) Hsu, A. L.; Herring, P. K.; Gabor, N. M.; Ha, S.; Shin, Y. C.; Song, Y.; Chin, M.; Dubey, M.; Chandrakasan, A. P.; Kong, J.; Jarillo-Herrero, P.; Palacios, T. Graphene-Based Thermopile for Thermal Imaging Applications. *Nano Lett.* **2015**, *15*, 7211–7216.

(42) Mao, J.; Shuai, J.; Song, S.; Wu, Y.; Dally, R.; Zhou, J.; Liu, Z.; Sun, J.; Zhang, Q.; Dela Cruz, C.; Wilson, S.; Pei, Y.; Singh, D. J.; Chen, G.; Chu, C. W.; Ren, Z. Manipulation of Ionized Impurity Scattering for Achieving High Thermoelectric Performance in *n*-Type Mg3Sb2-Based Materials. *Proc. Natl. Acad. Sci. U. S. A.* **2017**, *114*, 10548–10553.